Chapter 4

Synchrotron Spectrum of The Jet

4.1 Introduction

Information about the jet radio spectrum and its evolution can be crucial for distinguishing between various jet models. However, there are several aspects of VLBI which impede spectral studies of parsec–scale regions. Reliability of spectral information extracted from VLBI data depends on many factors including sampling functions at different frequencies, alignment of the images, calibration errors, narrow range of observing frequencies, and source variability. The influences of all these factors must be understood and, if possible, corrected for, in order to reconstruct the spectral properties of parsec–scale jets consistently.

In this chapter, we discuss three different approaches to studying synchrotron spectra in the jet: 1) spectral index mapping; 2) discrete spectral fitting; 3) continuous spectral fitting.

4.2 Spectral index mapping

Spectral index maps are produced by overlaying two VLBI images made at different frequencies (ν_1, ν_2) The spectral index

$$\alpha = a_1 \frac{\ln(S_1/S_2)}{\ln(\nu_1/\nu_2)} + a_2 \tag{4.1}$$

is calculated in every pixel with detected and validated emission at both frequencies. The scaling coefficients $a_{1,2}$ are usually ignored.

4.2.1 Spectral index mapping with VLBI

Spectral index mapping has been implemented and widely used in observations made with the scaled arrays. In such observations, the antenna configurations are selected at each frequency in a specific way such that the uv–coverages are identical. Unlike with linked interferometers, it is virtually impossible to use the scaled array technique and achieve identical *uv*–coverage for VLBI observations made at different frequencies. Uneven *uv*–coverage results in differences of the synthesized beams, and can ultimately lead to confusion and spurious features appearing in spectral index maps.

With larger number of antennas, the overlapping parts of the *uv*–coverages constitute an increasingly larger fraction of the joint *uv*–population. This results in decreasing the flux density level at which the confusion effects dominate the spectral index calculations. The confusion level can be lowered further by applying specific weighting schemes to the data (*uv*–tapering), and by matching the ranges of the *uv*–coverages at both frequencies. In the spectral index maps produced using the abovementioned procedures, confusion occurs at the flux level of about 0.3–0.5% of the mean peak flux density in the corresponding total intensity maps.

Figure 4.1 presents a spectral index map of 3C345 produced from the data at 8.4 GHz (1992.71) and 5 GHz (1992.42). On the jet limb, there are three areas of suspiciously high spectral index caused by remaining side lobes at the flux level of about 7 mJy per beam. The locations of the bright jet components are marked by the flat spectral index areas, in agreement with the shock interpretation of the jet enhanced emission regions. The map also shows a gradient of spectral index in the core. This gradient can reflect physical conditions in the core (or their changes; note the time separation between the observation epochs of the total intensity maps). The proper motion of superluminal components ($\sim 0.1 - 0.2$ mas) can also affect the spectral index map, although it is significant only for the most distant components. The observed gradient can also be due to the frequency dependent shift of the core position predicted by Königl (1981) and measured in 3C345 by Biretta, Moore, and Cohen (1986), and by Zensus, Cohen, and Unwin (1995). We will discuss the problem of frequency dependent shifts in Section 4.2.3.

4.2.2 Spectral index mapping with the VLBA

Many of the usual technical problems in making spectral index maps from VLBI data can be avoided by using the VLBA. With the VLBA, it is possible to achieve array homogeneity, have an improved flux calibration, and make the time separation between observations at different frequencies negligible. The major remaining problems are different *uv*–coverages and different spatial sensitivities. To overcome these difficulties, the following observation and data reduction scheme can be used:

1) Quasi–simultaneous multifrequency snapshot observations. The reliability of snapshots can be demonstrated by the comparison of the map of 3C345 and an image made from simulated data that were sampled so that they represent the *uv*–coverage typical for a snapshot–type observation (Figure 4.2). Despite some loss of dynamic range and sensitivity, the extended structure is still well detected in the simulated image. The jet appearance in the simulated image is consistent with the jet structures seen in the actual map.

For the snapshot–type observations, we have calculated the relations between

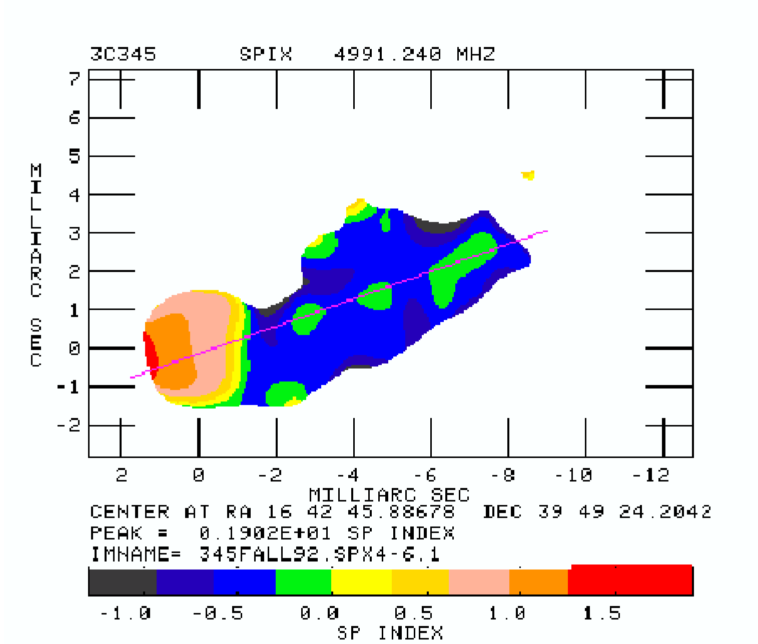

Figure 4.1: Spectral index map of 3C345 made between 8.4 and 5 GHz.

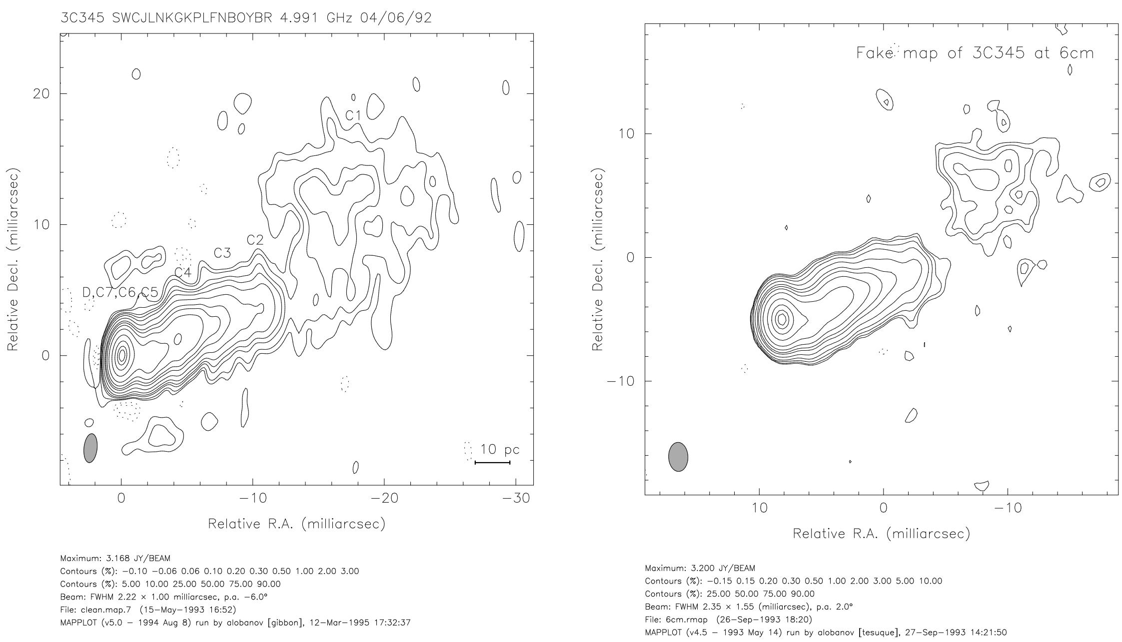

Figure 4.2: Real (left) and simulated (right) maps of 3C345 at 6cm.

Table 4.1: Maximum sampling intervals [min] for a 5000 km–long baseline.

λ (cm)	**structure size (mas)**								
	0.1	1	3	5	10	20	30	50	100
0.7	...	33	11	6.5	3.5	1.5	1.0	0.5	0.3
1.3	...	60	20	12	6.0	3.0	2.0	1.2	0.6
2.0	...	*95*	32	19	9.5	4.7	3.2	1.9	1.0
4.0	...	*190*	65	38	19	10	6.5	4.0	2.0
6.0	...	*290*	*95*	55	28	14	10	5.5	3.0
13	...	...	*200*	*120*	60	30	20	12	6.0
18	...	...	...	*190*	*95*	47	32	19	10
50	...	...	...	...	*240*	*120*	80	48	24
90	...	...	...	...	...	*210*	*140*	85	42

Table 4.2: Maximum detectable structure [mas] on a 5000 km-long baseline.

λ (cm)	**sampling interval (min.)**								
	10	15	20	25	30	35	40	50	60
0.7	3.3	2.2	1.7	1.3	1.1	1.0	0.8	0.7	0.6
1.3	6.0	4.1	3.0	2.4	2.0	1.8	1.6	1.2	1.0
2.0	9.5	6.5	4.7	3.8	3.2	2.7	2.4	1.9	1.6
4.0	19	12	9.5	7.5	6.5	5.5	4.7	3.8	3.2
6.0	28	19	14	11	9.5	8.0	7.0	5.5	4.7
13	60	41	30	24	20	18	16	12	10
18	95	65	47	38	32	27	24	19	16
50	240	160	120	95	80	70	60	47	40
90	430	280	220	170	140	120	100	85	70

Table 4.3: Maximum sampling intervals [min] for a 8600 km–long baseline.

λ (cm)	**structure size (mas)**								
	0.1	1	3	5	10	20	30	50	100
0.7	*190*	19	6.5	4.0	2.0	1.0	0.5	0.3	0.2
1.3	*360*	36	12	7.0	3.5	1.8	1.2	0.7	0.4
2.0	...	55	18	11	5.5	2.7	1.8	1.1	0.6
4.0	...	*110*	38	22	11	5.5	4.0	2.5	1.0
6.0	...	*160*	55	32	16	8.0	5.5	3.0	1.5
13	...	*360*	*120*	70	35	18	12	7.0	3.5
18	...	...	*180*	*110*	55	27	18	11	5.5
50	...	...	...	*280*	*140*	70	46	28	14
90	...	...	...	...	*240*	*120*	80	50	25

Table 4.4: Maximum detectable structure [mas] on a 8600 km-long baseline.

λ (cm)	sampling interval (min.)								
	10	15	20	25	30	35	40	50	60
0.7	1.9	1.3	1.0	0.8	0.7	0.6	0.5	0.4	0.3
1.3	3.5	2.4	1.8	1.4	1.2	1.0	0.9	0.7	0.6
2.0	5.5	3.8	2.7	2.2	1.8	1.6	1.4	1.1	0.9
4.0	11	7.0	5.5	4.4	3.8	3.2	2.7	2.2	1.8
6.0	17	11	8.0	6.5	5.5	4.6	4.0	3.2	2.7
13	35	24	18	14	12	10	9.0	7.0	6.0
18	55	38	27	22	18	16	14	11	9.0
50	140	95	70	55	47	40	35	28	23
90	240	160	120	100	80	70	60	50	40

sampling intervals and angular sizes of structures that can be detected using these intervals. The calculations have been done for medium VLBA baselines (5000 km), and for the longest available VLBA baseline (Saint Croix – Mauna Kea, 8600 km). The calculations are summarized in Tables 4.1–4.4. For every combination of wavelength and size, Tables 4.1,4.3 give the corresponding maximum allowed sampling interval [in minutes] between individual scans. Dots indicate that a structure remains unresolved. Italics highlight the 50% decrease of sensitivity. Tables 4.2,4.4 give the expected maximum size of detectable structure [in mas], for any given combination of wavelength and sampling interval.

In multifrequency observations, the sensitivity at each individual wavelength decreases, and this fact has to be taken into consideration in the case of mapping the weak extended emission. Figure 4.3 shows the decrease of sensitivity as a function of sampling interval.

It follows from Tables 4.1–4.4 and Figure 4.3 that multifrequency observations can provide satisfactory structure and flux sensitivities for bright sources with intermediate ($\approx$ 10 mas) extension. For such sources, full–scale spectral index mapping with 5 minute–long scans can be done at frequencies lower than 22 GHz (1.3 cm). Correspondingly, observations at three or more frequencies will require longer wavelengths.

2) Careful choice of wavelengths. The choice of wavelengths must be a compromise between the possibility of detecting the source structure and the VLBA sensitivity. Typically, at frequencies higher than 22 GHz, the requirements on brightness temperature limit the sensitivity. Also, there is a stronger dependence of the high frequency data on atmospheric instabilities. At frequencies lower than 2 GHz (13 cm), many sources will become too complicated to warrant a successful snapshot observation (see Tables 4.1–4.4).

3) Improvement in the flux calibration, due to frequent system temperature measurements and flat power gains of the VLBA antennas.

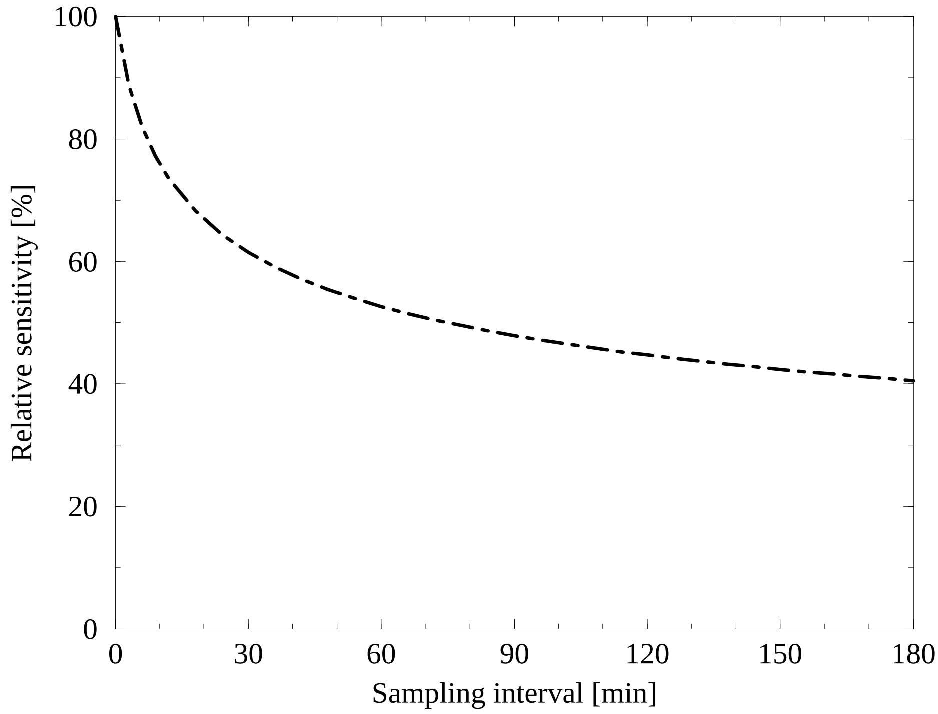

Figure 4.3: Relative loss of sensitivity in multifrequency observation. The calculations are done for 5 minute–long scans. Sampling interval reflects time separation between scans at the given frequency.

4) Applying appropriate uv–tapering, in order to provide matching uv-ranges for data taken at different frequencies.

5) Convolving data at different frequencies with the same, artificially circular beam.

6) Using SNR and flux threshold cutoffs, in order to leave out sidelobe induced artifacts.

7) If strong sidelobe effects remain, matching the uv–coverages within certain uv–ranges or over the whole uv–plane.

A spectral index map produced from two VLBA observations of 3C345 at 8.4 GHz (1993.88) and 5 GHz (1993.69) is shown in Figure 4.4. The confusion level of the map is about 4 mJy. The core contains a transversely extended region with $\alpha \approx 1$ which is likely to be associated with strong emission from the blend of C6 and C7. The preferred transverse direction of this and other features in the spectral index map indicate their possible relation to shocked emission. It can also be evidence of jet proper motion affecting the picture. Apart from the feature corresponding to C6-7, the jet does not contain other strong shocks. The emission from C2 (the most distant feature separated from the jet by a gap) is detected in a spectral index map for the

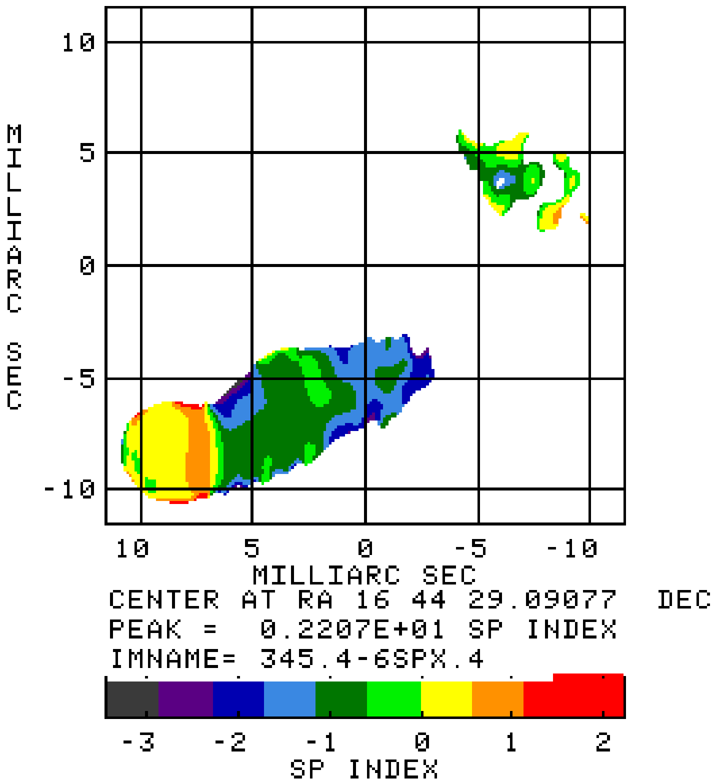

Figure 4.4: Spectral index map of 3C345 produced between 8.4 and 5 GHz.

first time. It is remarkable that its spectral index is consistently flat, supporting the hypothesis of a stationary shock used to explain the emission of C2 (see Unwin and Wehrle 1992, and Chapter 3.).

4.2.3 Image alignment

High-precision measurements of radio source absolute positions which are required for alignment of two VLBI images are not readily available in most cases. Extensive absolute astrometry (see Fomalont 1995) observations are necessary, in order to establish a reliable link between VLBI data at different frequencies. In quasi–simultaneous multifrequency observations, the phase–referencing technique (Beasley & Conway 1995) can be sufficient for the purpose of image alignment. If neither of the abovementioned techniques is available, VLBI images are usually aligned by the position of the source compact core.

Possible drawbacks of using the core for the alignment are evident from the analysis made by Königl (1981). Because the core is likely to be located in an optically thick environment, its position must depend on the observing frequency. According to Königl (1981), the jet emission can be detected at the separation r_{max} from the

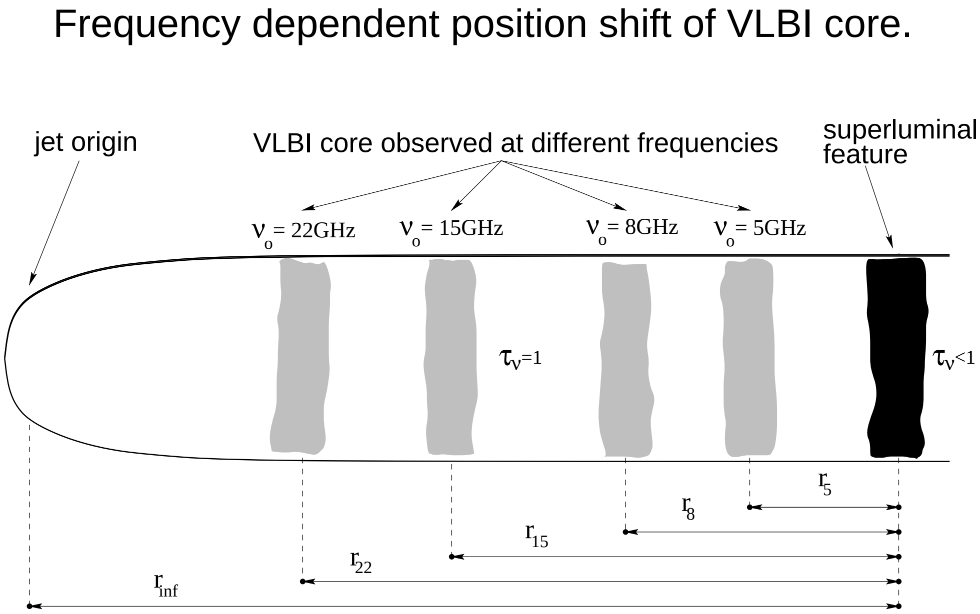

Figure 4.5: Shift of the observed VLBI core position: at any frequency, the core is seen at the location of the jet where its opacity to synchrotron self-absorption is $\tau_s = 1$. Farther down the jet, the emission is optically thin, and therefore the superluminal features are seen at the same locations at all frequencies.

true jet origin:

$$r_{max} \propto \nu^{-1/k_r}. \tag{4.2}$$

The term k_r is close to unity, so that r_{max} depends almost inversely on the frequency. Therefore, if aligned by the position of the core, VLBI images may contain systematic position offsets undermining spectral index mapping. We will discuss the physics of the VLBI core position shift in Section 6.2.3 of Chapter 6.

The frequency dependent shift of the core position can be deduced from comparison of observations made at close epochs, assuming that the superluminal features observed in the jet are optically thin and therefore should have their positions unchanged. In this case, the offsets between the component locations measured at different frequencies will reflect the frequency dependent shift of the position of the source core (Figure 4.5). In our data, there are three close pairs of VLBI observations: (1989.24 at 22.3 GHz)–(1989.26 at 10.6 GHz), (1992.44 at 22.3 GHz)–(1992.45 at 5 GHz), (1993.69 at 5 GHz)–(1993.72 at 22.3 GHz). The separations between the observations do not exceed 10 days, in these pairs. We also use two other close pairs with separations of 51 days: (1992.71 at 8.4 GHz)–(1992.86 at 22.3 GHz), and of 70 days: (1993.69 at 5 GHz)–(1993.88 at 8.4 GHz). We measure the position offsets for the closest and brightest components which are the most reliably detected by the model fitting. For the pairs with 51 and 70 days separation, component positions have been adjusted for the proper motions measured from the polynomial fits to the components trajectories (see Chapter 3).

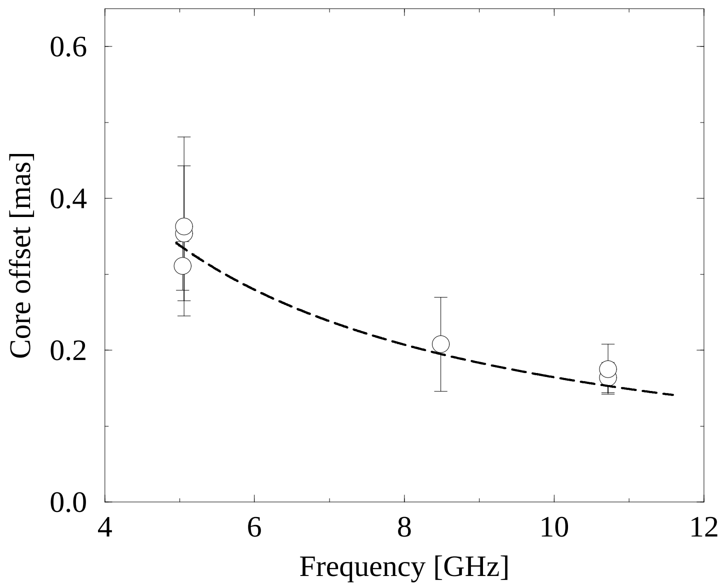

Figure 4.6: Frequency dependent shift of the core position in 3C 345. The reference frequency is 22.3 GHz. Dashed line corresponds to $r \propto \nu^{-1.04}$.

Figure 4.6 shows the measured offsets with respect to the reference frequency (chosen to be 22.2 GHz). The dashed line in Figure 4.6 represents the best fit:

$$r \propto \nu^{(-1.04 \pm 0.16)} \tag{4.3}$$

which is very close to the model prediction of Blandford and Königl (1979). The average angular offsets are compared in Table 1 with the optimal restoring beam sizes and pixel sizes of spectral index maps made from the corresponding frequency pairs. The offset position angles in Table 4.5 are similar to the position angle of the innermost part of the jet observed at 43 GHz (Zensus *et al.* 1996b). Between 5 and 8.4 GHz, the position shift is less than one pixel in the map, and it constitutes only about 2.5% of the restoring beam size. Therefore, we can expect that in the spectral index maps made between 5 and 8.4 GHz the effect of position shift will be negligible. With increasing frequency separation, the position shift exceeds the pixel size and constitutes a prominent fraction of the beamsize (up to 27% for maps between 5 and 22.3 GHz).

4.2.4 Spectral index maps

We apply the frequency dependent shift to three spectral index maps made between 10.6 and 22.3 GHz (1989.25), and between 5 and 22.3 GHz (1992.45, 1993.70). The resulting pictures are given in Figures 4.7–4.11. The unshifted core position in the

Table 4.5: Average offsets of the core position

1	2	3	4	5	6	7
Frequency pair	Δr [mas]	Δr_p [pix]	$b_{\Delta r}$	$\Delta\phi$ [deg]	Δr_{proj} [pc]	$\Delta r_{\theta=5}$ [pc]
5 – 8.4 GHz	0.05 ± 0.02	1	5%	-70.8 ± 4.1	0.1	1.2
10.6–22.3 GHz	0.17 ± 0.04	3	20%	-73.5 ± 2.0	0.6	7.5
8.4–22.3 GHz	0.21 ± 0.06	4	20%	-71.4 ± 1.4	0.8	9.1
5–22.3 GHz	0.33 ± 0.02	6	28%	-77.1 ± 2.6	1.2	14.3

Notes: 2 – offset in mas; 3 – offset in pixels; 4 – offset as a fraction of the restoring beam of the corresponding spectral index map; 5 – offset position angle; 6 – projected linear distance corresponding to the offset; 7 – corresponding length of a jet with angle to the line of sight $\theta = 5^{\circ}$.

maps is (3,0). In each pair of maps constituting a spectral index map, the offset was applied to the map at the lower frequency.

10.6–22.3 GHz map. (1989.25)

The unshifted map shown in the top panel of Figure 4.7 has a significant negative transversal gradient of spectral index towards the northern side of the jet. In the core, the spectral index is higher on the edge (see the spectral index profiles in Figure 4.8), which is an indication of possible position errors. In the corrected map (bottom panel in Figure 4.7) the source edge has negative spectral index, and the maximum spectral index is located in the core. The gradient on the northern side of the jet has diminished. The low spectral indices on the very limb of the jet may result from flux errors due to the low dynamic range of the total intensity maps.

C4 is located approximately at the position: (1.4, –0.7), marked by the area of higher spectral index. The positive spectral index observed for the component may suggest the presence of a shock. Because of the relatively poor match between the *uv*–coverages, the observed effect can also be caused by the difference of spatial sensitivities at 10.6 and 22.3 GHz.

Nevertheless, the map illustrates well the effect of correction for frequency dependent shift. It shows that some of the supposedly erroneous features (significant transversal gradients, high spectral index on the edges) can be removed by applying the measured core offset between the constituent pair of frequencies.

5–22.3 GHz map (1992.45)

In the map at 22.3 GHz (see Figure 2.11 in Chapter 2), C7 has very high flux density which causes a 0.1 mas westward shift of the phase center of the map. This shift was also accounted for during the core offset correction. The unshifted spectral index map (top panel of Figure 4.9), shows a spectral index gradient in the core, with the maximum located at the edge (see the corresponding profiles in Figure 4.10). In

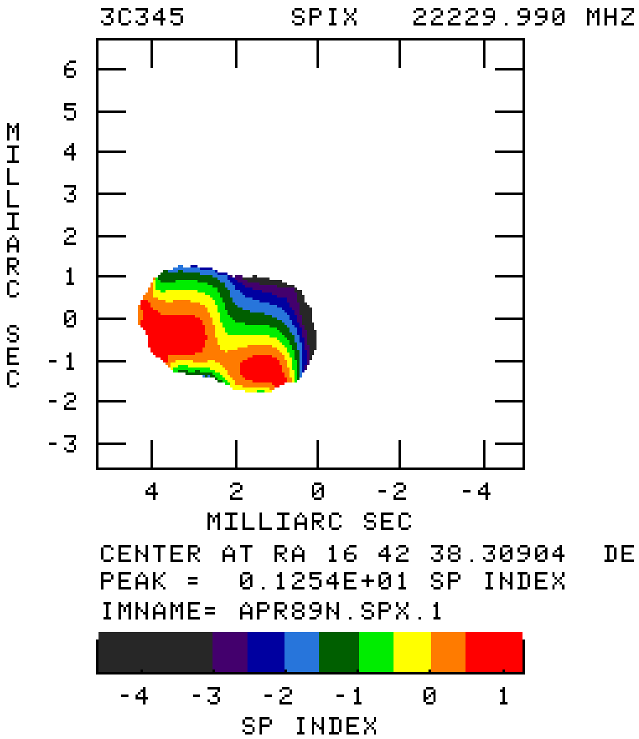

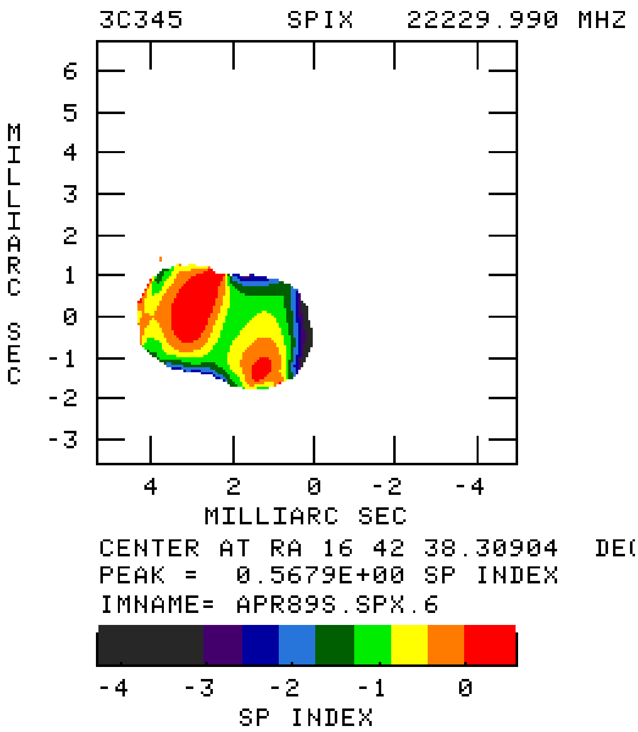

Figure 4.7: Spectral index maps of 3C345 made between 10.6 and 22.3 GHz (epoch: 1989.25). Top panel shows the original map, bottom panel shows the map corrected for the frequency dependent shift of the core position.

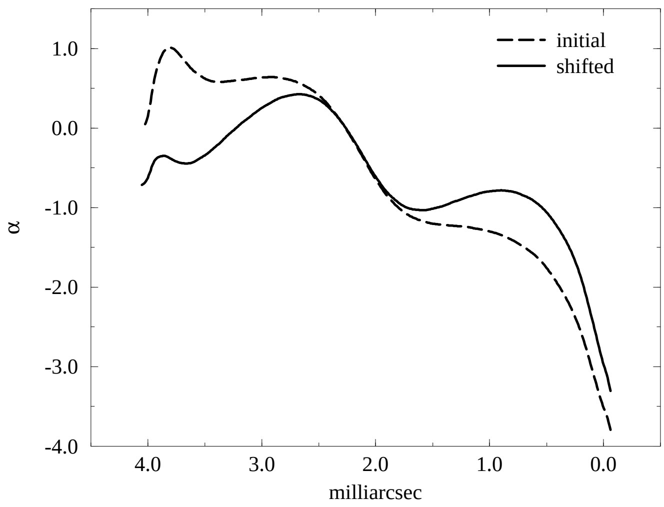

Figure 4.8: Spectral index profiles for the epoch 1989.26. The profiles are taken along the relative declination $\delta = 0$ mas. Dashed line gives the profile for the unshifted map, solid line presents the profile for the shifted map. The location of the core corresponds to 3 mas offset.

the corrected map (lower panel of Figure 4.9) the maximum value of spectral index corresponds to the location of C7 which was, in 1992.45, the strongest feature at 22.3 GHz. Positive spectral indices of the core and C7 are likely to be related to the outburst occuring in 3C345.

The spectral index distribution in the extended regions of the jet is affected insignificantly by the shift. This indicates that extended emission is distributed more smoothly at 5 GHz, so that changes of the spectral index are determined largely by the flux variations at 22.3 GHz.

5–22.3 GHz map (1993.45)

In 1993, the core and C7 were in a more quiescent state, compared to 1992 (see the corresponding model fits in Chapter 2). In the images used for producing the spectral index map, the core, C7, and C6 are blended together (since the size of restoring beam is 1.2 mas, in these images). From the Gaussian models, crude estimates of the 5–22.3 GHz surface brightness ratio of the area within ≈1 mas around the core give $B_{22\,GHz}/B_{5\,GHz} \approx 1.2$. This should result in a measured flat spectral index distribution $\alpha \approx 0.1$, for the emitting complex consisting of C6, C7, and the core.

In the unshifted spectral index map (top panel of Figure 4.11), there is, however, a strong gradient across the core (see the corresponding spectral index profile in Figure 4.12). The spectral index changes roughly from -1 to $+1$ across the core complex. The distribution of spectral index is practically transverse to the jet position angle,